



**HAL**  
open science

## The mechanical properties of the Martian soil at the InSight landing site

Pierre Delage, E Marteau, C Vrettos, M Golombek, V Ansan, W B Banerdt, M Grott, Kenneth Hurst, P Lognonné, N Murdoch, et al.

► **To cite this version:**

Pierre Delage, E Marteau, C Vrettos, M Golombek, V Ansan, et al.. The mechanical properties of the Martian soil at the InSight landing site. Proceedings 20th International Conference on Soil Mechanics and Geotechnical Engineering, Sydney, May 2022, May 2022, Sydney, Australia. hal-03706564

**HAL Id: hal-03706564**

**<https://hal.science/hal-03706564>**

Submitted on 27 Jun 2022

**HAL** is a multi-disciplinary open access archive for the deposit and dissemination of scientific research documents, whether they are published or not. The documents may come from teaching and research institutions in France or abroad, or from public or private research centers.

L'archive ouverte pluridisciplinaire **HAL**, est destinée au dépôt et à la diffusion de documents scientifiques de niveau recherche, publiés ou non, émanant des établissements d'enseignement et de recherche français ou étrangers, des laboratoires publics ou privés.

# The mechanical properties of the Martian soil at the InSight landing site

## Les propriétés mécaniques du sol martien sur le site de la mission InSight

Delage<sup>1</sup> P., Marteau<sup>2</sup> E., Vrettos<sup>3</sup> C., Golombek<sup>2</sup> M.P., Ansan<sup>4</sup> V., Banerdt<sup>2</sup> W. B., Grott<sup>5</sup> M., Hurst<sup>2</sup> K., Lognonné<sup>6</sup> P., Murdoch<sup>7</sup> N., Piqueux<sup>2</sup> S., Schmelbach<sup>8</sup> C., Spohn<sup>5,9</sup> T., Warner<sup>10</sup> N., Widmer-Schmidrig<sup>11</sup> R., Brinkman<sup>8</sup> N., Caicedo-Hormaza<sup>12</sup> B., Castillo-Betancourt<sup>1,12</sup> J.P., Edme<sup>8</sup> P., Kedar<sup>2</sup> S., Lange<sup>13</sup> L., Lemmon<sup>2</sup> M., Mueller<sup>5</sup> N., Onodera<sup>6</sup> K., Robertsson<sup>8</sup> J., Sollberger<sup>8</sup> D., Stähler<sup>8</sup> S., Verdier<sup>14</sup> N., Williams<sup>2</sup> N.R.

<sup>1</sup> Ecole des Ponts ParisTech, Laboratoire Navier/CERMES, CNRS, Marne la Vallée, France

<sup>2</sup> Jet Propulsion Laboratory, NASA - California Institute of Technology, Pasadena, CA, USA

<sup>3</sup> Technical University of Kaiserslautern, Department of Civil Engineering, Germany

<sup>4</sup> Nantes Université, Laboratoire de Planétologie et Géodynamique, CNRS, Nantes, France

<sup>5</sup> DLR Institute of Planetary Research, Berlin, Germany

<sup>6</sup> Université de Paris, Institut de Physique du Globe de Paris, CNRS, Paris, France

<sup>7</sup> ISAE – SUPAERO, Toulouse, France

<sup>8</sup> ETH Zürich, Institute of Geophysics, Department of Earth Sciences, Switzerland

<sup>9</sup> International Space Science Institute, Bern, Switzerland

<sup>10</sup> SUNY Geneseo, Department of Geological Sciences, Geneseo, NY, USA

<sup>11</sup> University of Stuttgart, Black Forest Observatory, Institute of Geodesy, Wolfach, Germany

<sup>12</sup> Universidad de los Andes, Bogota, Colombia

<sup>13</sup> Sorbonne Université, Laboratoire de Météorologie Dynamique, CNRS, Paris, France

<sup>14</sup> Centre National d'Études Spatiales, Toulouse, France

**ABSTRACT:** The InSight mission is a NASA geophysical mission aimed at better understanding the structure of Mars and of the other rocky planets of the solar system. To do so, various instruments are used, including a very sensitive seismometer (SEIS) and a dynamic self-penetrating heat probe (HP<sup>3</sup>) that have been placed on the Mars surface by the Instrument Deployment Arm (IDA). Besides geophysical data (which have definitely enriched and completed existing knowledge on the structure of Mars), the InSight instruments, together with orbiter observations and tests carried out on the soil with the IDA, have significantly increased the knowledge of the geological and geotechnical characteristics of the surface material at the InSight site, which is made up of a basaltic sand. In-situ data were also successfully compared with terrestrial previous estimates from terrestrial lab tests, carried out on various soil simulants. Small strain (elastic) parameters at small strains were derived from wave velocity measurements between the self-penetrating probe and the seismometer. Strength data were derived from both IDA operations and penetration data. The soil includes some pebbles within a somewhat cohesive sandy matrix, limiting the heat probe penetration to only 40 cm length. Thermal data were also obtained, allowing for some thermo-elastic modelling of the effect of the Phobos (one of the “Moons” of Mars) eclipses. Elastic data were also derived from the effects of wind on the ground, detected by SEIS.

**RÉSUMÉ :** La mission InSight est une mission géophysique de la NASA destinée à mieux comprendre la structure de Mars et des planètes telluriques du système solaire à l'aide de divers instruments, incluant un sismomètre ultra-sensible et une sonde de pénétration dynamique destinée à des mesures thermiques, qui ont été placés sur le sol de Mars par un bras robotisé. À côté des données géophysiques obtenues (qui ont largement enrichi et complété la connaissance de la structure de la planète), les données fournies par les instruments, complétées par des observations satellitaires et des essais réalisés par le bras robotisé sur le sol, ont permis d'élargir considérablement la connaissance des caractéristiques géologiques et géotechniques du sol martien du site d'InSight, constitué de sable basaltique. Les données obtenues in-situ ont aussi été favorablement comparées à celle estimées préalablement sur Terre par des essais de laboratoire sur des analogues de sol martiens. Les paramètres élastiques à petites déformations ont été obtenus à partir de mesures de vitesses d'ondes sismiques entre la sonde et le sismomètre, lors des opérations de pénétration dynamique en surface. Des caractéristiques à la rupture ont été obtenues par les sollicitations exercées sur le sol par le bras robotisé et par les données de pénétration. Le sol s'est révélé être composé de cailloux contenus dans une matrice sableuse légèrement cohérente, ce qui n'a rendu la pénétration de la sonde thermique possible que sur les 40 cm de sa longueur. Des données thermiques ont aussi été obtenues, permettant la modélisation thermo-élastique des déformations induites par une éclipse de Phobos, une des 'Lunes' de Mars. Des données élastiques ont été aussi déduites des effets du vent sur la surface, détecté par le sismomètre.

**KEYWORDS:** Mars, geophysics, regolith, seismometer, heat probe, seismic waves, elastic parameters, penetration, strength

### 1. INTRODUCTION

The investigation of the mechanical properties of the surface deposits on Mars has been considered in details since the landing of Vikings 1 and 2 in 1976 (e.g. Moore and Jakoski 1989) and completed based on the data obtained from landers and rovers of other missions (see Christensen and Moore 1992, Golombek et al. 2008, Herkenhoff et al. 2008).

The InSight mission on Mars (Interior Exploration using Seismic Investigations, Geodesy and Heat Transport, Banerdt et al. 2020) is a geophysical mission managed by NASA and aimed at better understanding the structure of Mars and of the other terrestrial planets of the Solar system. Just to recall, Mars is one of the four terrestrial planets of the Solar system, with a Martian year around as long as twice the Earth year, an average diameter of 6 779 km (0.553 that of the Earth) and, as a result, a smaller

gravity of  $3.711 \text{ m/s}^2$ . The atmosphere on Mars is mainly composed of  $\text{CO}_2$  with an average atmospheric pressure of 610 Pa.

The main geophysical instruments deployed by the InSight mission on Mars are i) a very-high-sensitivity seismometer (SEIS, Lognonné et al. 2019, 2020), including a very-broad-band seismometer (VBB) funded by the French Space Agency (CNES) and a short-period (SP) one developed at Imperial College and ii) the HP<sup>3</sup> instrument (Heat flow and Physical Properties Package, Spohn et al. 2018) a device designed that includes a self-penetrating dynamic cylindrical probe (40 cm long and 2.7 cm diameter) nicknamed the mole and funded by the German Space Agency (DLR). The HP<sup>3</sup> instrument is designed to perform thermal conductivity and thermal gradient measurements along the first 3 – 5 meters below the surface, from which the heat flow from of the interior of the planet could be calculated. To do so, the mole was supposed to drag down a captor tether (Spohn et al., 2018).

The InSight lander also carries a weather station monitoring the changes in temperature, atmospheric pressure and wind. The InSight lander the successfully landed on Mars in western Elysium Planitia on 26 November 2018 (NSY in Figure 1), a little bit north of the equator. This first day of the mission is defined as sol 1: a sol is a Martian day, about 40 minutes longer than an Earth day. Figure 1 also shows the landing sites of the Viking 2 Lander (VL2, 1976), in Utopia Planitia, of the Mars Science Laboratory (MSL) Curiosity rover in the Gale crater (2012) and the Mars Exploration Rover (MER) Spirit in Gusev crater (2004). InSight landed on ~200 m thick lava flows from Early Amazonian-Hesperian period (1.8-3.6 billion years), underlain by sedimentary rocks of likely Noachian age (around >3.6 billion years, Pan et al. 2020) possibly containing phyllosilicates.

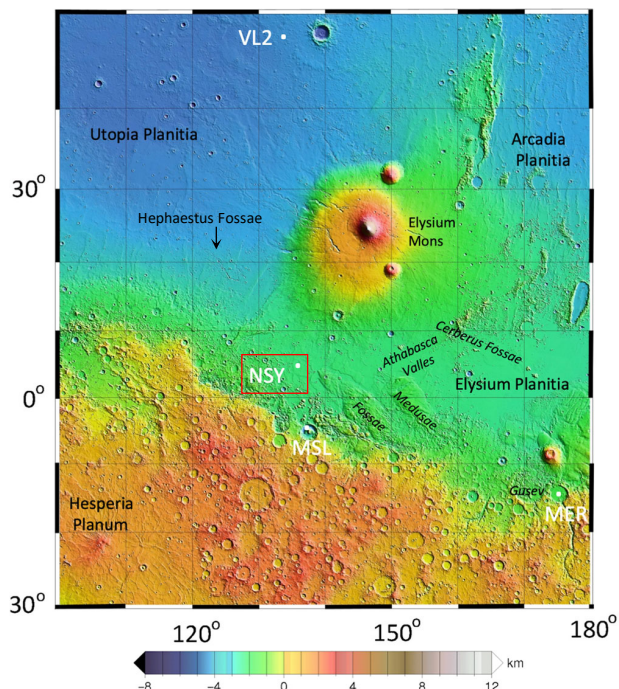


Figure 1. Locations of the InSight lander (NSY) close to the equator ( $4.502^\circ\text{N}/135.623^\circ\text{E}$ ), not far from the dichotomy boundary that separates, on Mars, the southern heavily cratered highlands from the northern lowlands (see color scale). The location of Hesperia Fossae (see Figure 6) is also indicated. The map is a portion of the Mars Orbiter Laser Altimeter (MOLA) shaded topographic map of Mars (after Golombek et al. 2018).

The artist view of the InSight lander (Figure 2) shows both the SEIS (covered by a wind and thermal shield) and the HP<sup>3</sup> instruments deployed. Both are linked to the lander by tethers that transmit energy and data. The Figure also shows the 2 m long

Instrument Deployment Arm (IDA) and its grapple that deployed both SEIS and HP<sup>3</sup> on the ground (Třebi-Ollennu et al., 2018). The IDA also carries a medium-resolution Instrument Deployment (colour) Camera (IDC). The lander is also equipped with a wide-angle Instrument Context Camera (ICC), a meteorological station including temperature, windspeed and pressure sensors, two X-band RISE antennas (Rotation and Interior Structure Experiment) providing a precise location of the lander to accurately monitor the movements of the planet from the Earth (Folkner et al. 2018, Golombek et al., 2020c), together with an Ultra High Frequency antenna for data transmission. Energy is provided by two twin 1.8-m diameter solar panels with a power of 700 W each, on clear days.

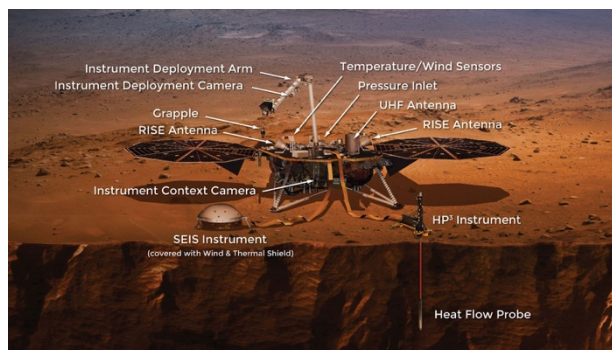


Figure 2. InSight lander artist's concept showing its scientific payload. <https://mars.nasa.gov/insight/spacecraft/instruments/summary/>

SEIS is a high-sensitivity inertial accelerometer, that has yielded impressive geophysical results in the detection of seismic signals and impacts on the planet since landing (Giardini et al. 2020). As an inertial accelerometer, SEIS is also sensitive to tilts that change the projection of the gravity vector onto the measurement direction of the accelerometer. In acceleration, its ASD (amplitude spectral density) noise floor in the band 0.01 - 2 Hz is slightly below  $1 \text{ (nm/s}^2\text{)/}\sqrt{\text{Hz}}$ . It can therefore act both as a very sensitive tilt meter and a seismometer, identifying the consequences of various mechanical actions like those due to changes in atmospheric pressure due to wind and dust devils (small local storms), temperature changes (including those from the eclipse caused by Phobos, one of the two Mars moons) or interactions between the IDA or the mole and the regolith. Some of these will be considered in this paper. Further actions are planned, like for example the monitoring by SEIS of a vertical force applied by the IDA to the ground, with the scoop used as an indenter.

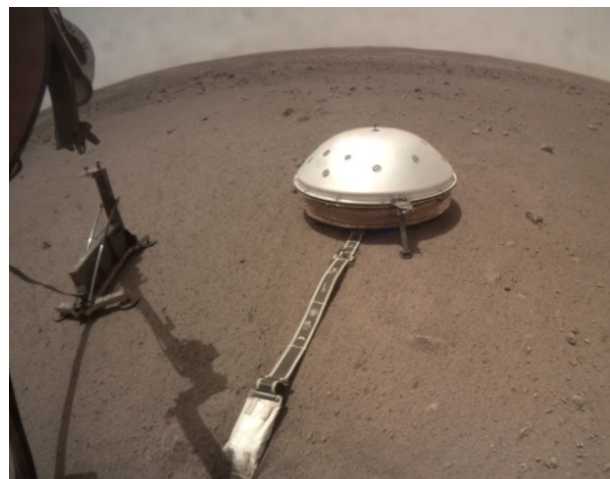


Figure 3. Photo taken from the Instrument Context Camera (ICC) showing the location of SEIS and of the HP<sup>3</sup> support structure, 1.18 meter apart from each other (image credit JPL/NASA).

Figure 3 shows both the HP<sup>3</sup> surface structure containing the mole and the SEIS covered by the thermal and wind shield, both having been successfully deployed by the IDA close to the lander. The distance between them is close to 1.1 m. Note that the waves emitted by the HP<sup>3</sup> driving system have been detected by SEIS, providing interesting information about wave velocities and elastic properties at the surface (see below). Note also that, as discussed in details in Spohn et al. (2021a), it has not been possible to drive the mole as deep as planned enough due to unexpected lack of friction with the regolith, to counteract the rebound occurring in the self-penetrating system during dynamic penetration. The mole only barely buried its entire length (40 cm), which still allowed wave velocity measurements (Lognonné et al. 2020, Brinkman et al. 2022) and thermal conductivity measurements near the surface (Grott et al. 2021). In an attempt to help the mole penetration, the HP<sup>3</sup> surface structure observed in Figure 2 and Figure 3 has been withdrawn by the IDA, revealing a pit that developed around the mole during the many hammering sessions carried out. The IDA was afterwards used to fill the pit with regolith so as to improve the regolith/mole friction, and to apply some pressure aimed at facilitating penetration, as seen below in Figure 8. All these attempts were unfortunately unsuccessful.

Figure 4 shows two selfies reconstituted from images taken by the IDC just after landing (the SEIS and HP3 instruments are still on the lander) and after around 100 days, with evidence of dust coating on the lander and the solar panels. Dust coating of the solar panels is quite an issue since it results in a regular decrease of the available power. As further commented below, it also confirms the presence of very fine particles transported by Mars winds.

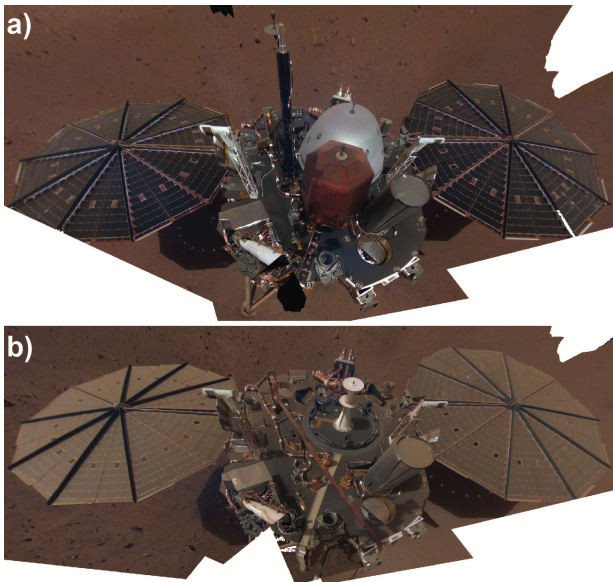


Figure 4. Comparative selfies of the InSight lander reconstituted from images taken by the IDC: a) at the beginning of the mission (Dec. 6, 2018, sol 10), with the instruments (SEIS and HP3) still on the lander; b) after around 100 days (March 15, 2019, sol 106 and April 11, 2019, sol 133), with evidence of dust coating on the lander and solar panels (Image credit JPL/NASA).

## 2. CHARACTERISATION OF THE SURFACE REGOLITH

The InSight landing site was selected from orbiter observations including high-resolution images from the HiRISE camera (Golombek et al. 2017). It was chosen for its smooth, flat relatively rock free surface mainly composed of sand-like regolith.

The regolith was formed by the long-term and successive impacts of meteors into the lava flows of Elysium Planitia, that progressively broke the basalt parent rock into smaller and smaller rocks and particles, to end up with a sand-like surface regolith.

This formation process can be illustrated by the HiRISE image (Figure 5, see location in Figure 1) of a steep scarp of Hephaestus Fossae exposure, a fracture ~900 km northwest of the InSight landing site that cuts through a potentially analogous terrain (Golombek et al. 2018). The photo shows ~ 4-5 m thick, relatively fine-grained regolith overlying blocky ejecta that grades into strong, jointed bedrock. Given that the bedrock is composed of basalt lava, the regolith is mainly basaltic as well.

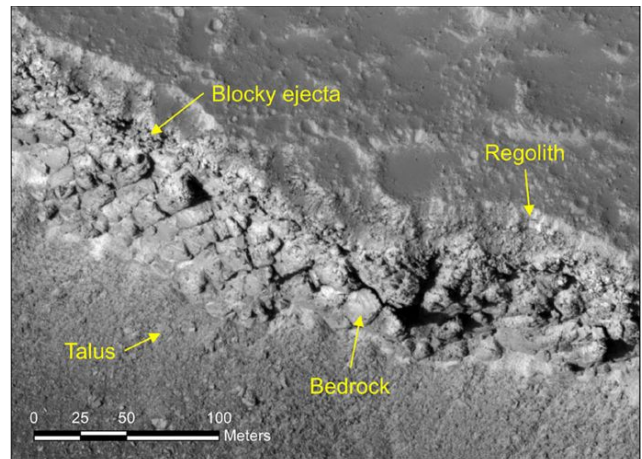


Figure 5. A portion of the exposed steep scarp of Hephaestus Fossae in southern Utopia Planitia (Golombek et al. 2018).

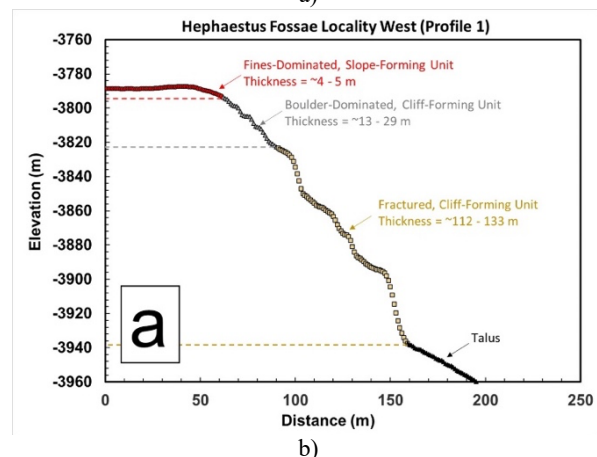
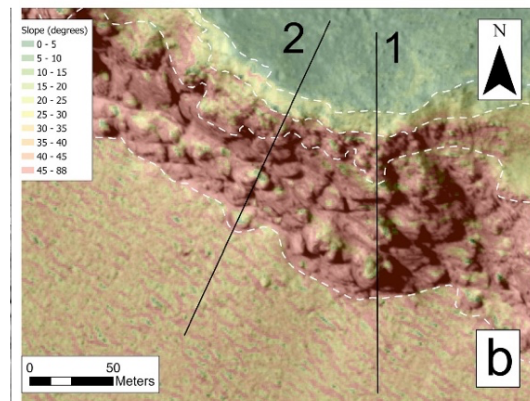


Figure 6. a) HiRISE image (ESP\_052638\_2020) of the Hephaestus Fossae exposure, a fracture ~900 km northwest of the InSight landing site; b) Slopes determined along profile 1 (Warner et al. 2022a, b).

As shown in Figure 6, (Warner et al. 2022a, b), the profile has been further analyzed, showing, on the top, a 4 – 5 m thick fines-dominated layer (with a maximum slope of 20°, smaller than the angle of repose estimated at 30°), underlain by a 13 – 29 m thick boulder-dominated cliff-forming unit, underlain by another cliff-forming unit (112 – 133 m thick) that may be the primary bedrock, with a talus at its base inclined at 32° (close to the estimated angle of repose of loose granular materials). The estimation of the grain distribution of the talus material is not straightforward, but it is probable that it is composed from part of fine regolith that flowed down from the top, together with other rocky debris with size comprised between 1 and 10 m coming from the upper layer of blocky ejecta. The entire stratigraphic sequence is consistent with an impact-comminuted lava plain with a gardened regolith that is up to 10 meters thick. The regolith fines upwards, a result of the higher frequency of small (order of 1 to 10 m) impacts.

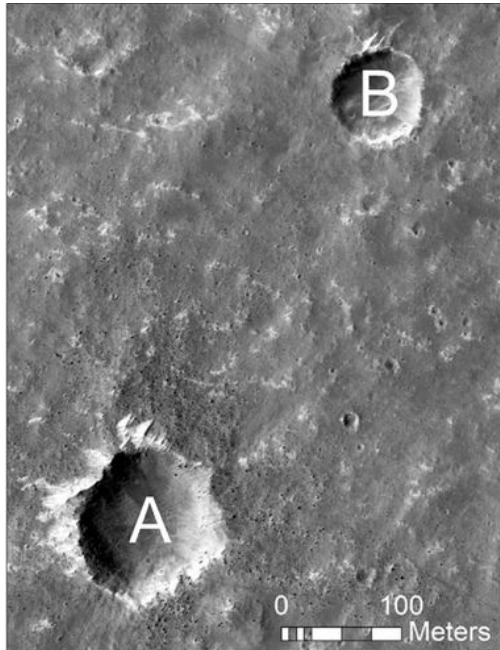


Figure 7. HiRISE image showing fresh crater A (112 m diameter), with rocky ejecta around and B (75 m) with no rocky ejecta around. The depth at which ejecta is sourced in fresh craters is 0.084 times the diameter (Golombek et al. 2017). Note that Golombek et al. (2020b) has a more specific treatment of the regolith depth.

In selecting the best landing site (Golombek et al. 2017), one challenge was to make sure that the thickness of the surficial regolith layer was larger than the 5 m depth at which the mole was planned to be driven. This was done by considering the various fresh craters located in the area of interest, and to check whether or not they had rocky ejecta around. In Figure 7, the small black dots around crater A (112 m diameter) are rocky ejecta, indicating that the meteorite hit the bedrock. This is not the case of crater B (75m diameter). As recalled by Golombek et al. (2017), observations of fresh craters show that the ratio between their depth and diameter is around 0.084 (75 x 0.084 = 6 m). Thus, the rocks around crater A have been extracted from a depth of around 9 m. So, the average regolith thickness in the area is between 6 and 9 m, which is satisfactory for driving the mole.

A significant feature of the regolith on Mars, compared to those of other terrestrial planets or bodies of the solar system where there is no atmosphere, is that surface particles are entrained in the wind, with an average atmospheric pressure of 610 Pa (Spiga et al., 2018; Banfield et al., 2020). Wind effects result in saltation, in which sand particles are moved in parabolic

hops by the wind. Particles have been shaped, transported and accumulated either in aeolian bedforms or in depressions like the so-called Homestead Hollow, in which the lander is located. As a consequence, soil particles on Mars are rounded to subrounded, as will be discussed below in more details (Golombek et al., 2020d).

Based on the formation mode described above and on geological observations from various previous Martian missions, the density of the sandy regolith of the InSight landing site is estimated to be low, with values between 1.1 and 1.4 Mg/m<sup>3</sup>, as shown in Table 1, that describes the nature and properties of various surficial soil type deposits on Mars (Golombek et al. 2008, Ch. 8). The mechanical properties have been derived from scraping, trenching and dumping experiments carried out with scoops as well as interactions with rover wheels. The Table also provides the properties of drift, or dust, a very fine material with particle size between 1 and 10 μm, that will be further discussed below.

Table 1. Characteristics of some Martian surface materials (after Golombek et al. 2008)

Material	Bulk Density Mg/m <sup>3</sup>	Grain Size μm	Cohesion (kPa)	Friction Angle °	Thermal Inertia <sup>1</sup>
Drift	1–1.3	1–10	0–3	15–21	40–125
Sand	1.1–1.3	60–200	0–1	30	60–200
Crusty to cloddy sand	1–1.6	5–500	0–4	30–40	200–326
Blocky, indurated soil	1–1.2	50–3000	31–11	40–60	369–410

See definition in main text; units are J m<sup>-2</sup> K<sup>-1</sup> s<sup>-1/2</sup>

### 2.1. Thermal inertia measurements

The average size of the regolith particles on Mars was initially estimated from thermal inertia measurements, which have been conducted from orbit - including those of the THEMIS (Thermal Emission Imaging System) instrument on board of the Mars Odyssey spacecraft launched in 2001 (e.g., Kieffer et al., 1977; Paluconi & Kieffer, 1981; Mellon et al., 2000; Putzig & Mellon, 2007; Golombek et al., 2008, Edwards et al. 2018) - and from the ground (Fergason et al., 2006; Golombek et al., 2020a; Hamilton et al., 2014).

The principle that allows derivation of average particle size from thermal inertia is simple: for the same mass, the changes in temperature of a particle (the average temperature of the atmosphere on Mars changes as much as 100°C between days and nights) are slower for larger particles (small specific surface) and faster for small particles (high specific surface). This trend is clearly observed in the data of Table 1. Note however that intergrains cementation in slightly cohesive granular materials may increase the thermal inertia.

Thermal inertia  $\Gamma$  (unit Jm<sup>-2</sup>K<sup>-1</sup>s<sup>-1/2</sup>) is given by:

$$\Gamma = \sqrt{k\rho c_p} \quad (1)$$

where  $k$  is the thermal conductivity,  $\rho$  the density, and  $c_p$  the specific heat capacity. While density and specific heat capacity vary little for different soils, thermal conductivity can vary by orders of magnitude, depending on bulk porosity, composition, grain size and the state of cementation or induration.

At the InSight landing site, orbital thermal inertia measurements indicated values between 160 and 230 J m<sup>-2</sup> K<sup>-1</sup> s<sup>-1/2</sup> (Golombek et al. 2020a), which were later confirmed by local measurements using the InSight HP<sup>3</sup> Radiometer (Spohn et al. 2018, Golombek et al. 2020a, Müller et al. 2020, Piqueux et al. 2021). Such thermal inertias correspond to thermal conductivities of  $0.041 \pm 0.013$  W m<sup>-1</sup> K<sup>-1</sup>, consistent with direct thermal conductivity measurements using the HP<sup>3</sup> mole as a modified

line heat source (Grott et al. 2019, 2021), which yielded thermal conductivities of  $0.039 \pm 0.002 \text{ W m}^{-1} \text{ K}^{-1}$  for the upper 3–37 cm of the soil. Due to low atmospheric pressure and gravity typical of Mars, these are very low values compared to those of current terrestrial soils, where  $k$  is close to 1.

Assuming the soil to be cohesionless and non-cemented, the above thermal conductivity values indicate that 85%–95% of all particles are smaller than 104–173  $\mu\text{m}$  (Grott et al. 2021). It is worth noting, however, that if cementation plays a significant role, this estimate needs to be viewed as an upper limit (Piqueux and Christensen, 2009). In that case, the volume of bonding between the grains has been modelled to be substantially less than 1% in volume (Piqueux et al. 2021).

As will be seen below, various observations show that, besides the average particle size estimated from thermal inertia measurements, a significant proportion of finer particles (including dust) exist in the surface layers of Mars, similar to those observed on the solar panels (see Figure 4b) and transported by winds.

### 2.2. Density Estimate from thermal conductivity

Previous geological observations suggested that the regolith density on Mars is low, with density estimated between 1.1 and 1.3  $\text{Mg/m}^3$  for sand-type regolith (see Table 1). While there are no direct measurements of soil density at the InSight landing site, some constraints may be derived based on the thermal measurements performed by the HP<sup>3</sup> TEM-A (Thermal Excitation and Measurement-Active mode, Grott et al. 2021). While these measurements are aimed at deriving thermal conductivity using a modified line heat source approach, the full inversion of the data also contains information on the soil thermal diffusivity  $\kappa = k/\rho c_p$  and thus the soil density. Values of soil density compatible with TEM-A measurements are  $1.211^{+0.149}_{-0.113} \text{ Mg/m}^3$ , in accordance with estimates of Table 1. This corresponds to a significant soil porosity of the order of  $63 \pm 4\%$  (Grott et al. 2021). This value is in excess of the value of 42% appropriate for a random loose packing, indicating that soil cohesion has played a role during soil deposition, enhanced by low gravity.

## 3. DIRECT OBSERVATIONS ON MARS

Figure 8 presents an IDC photo of the scoop of the Instrument Deployment Arm (IDA) compressing the regolith above the hole that developed around the self-penetrating mole during hammering, with the tether appearing on the left side of the scoop.



Figure 8. IDC photo showing the scoop of the Instrument Deployment Arm compressing the regolith, once the pit filled. The tether appears on the left side. The scoop width is 7.6 cm (image credit JPL/NASA).

The photo confirms the sand-like aspect of the surface regolith, with no rock in the area and some centimeter-sized pebbles around. Note also the perfectly smooth imprint of the scoop observed between the right side of the scoop and the elongated pile on the right. Such smooth surfaces have also been observed on rover tracks in other missions and indicate that the fine particles contained in the sandy layer provide some degree of cohesion (Golombek et al. 2020a) that will be further discussed later on. As in other Martian missions since those performed from the Viking lander (Moore et al. 1982, 1987, Moore and Jakosky 1989) and as shown below, the scoop has been used to perform scraping, trenching and piling operations, from which some soil mechanics parameters have been derived.

It is well-known that the surface of Mars is regularly covered by small particles of dust with size of a few microns (2–5  $\mu\text{m}$ ) similar to those observed on the solar panels (see Figure 4b). Dust is transported over thousands of kilometers during regional to global dust storms (e.g., Cantor, 2007). During the InSight mission, a regional dust storm occurred (e.g., Viudez-Moreiras et al. 2020). Note that the deposition of this red dust on the solar panels of rovers and landers has serious consequences on their energy supply, including for the InSight lander (Figure 4). Actually, orbiter observations indicated that a thin layer (<1 cm thick) of dust was removed by the rockets during landing to an average distance of 20 m around the InSight lander (Golombek et al. 2020a, b). So, the average 170  $\mu\text{m}$  diameter particles estimated from thermal inertia is only a global indication about grain sizes, and smaller particles also exist in the regolith.

Further evidence on the nature of the regolith particles on Mars has been provided by the microscopic imagers of the Spirit, Opportunity and Curiosity rovers, the Phoenix lander and by the atomic force microscope of the Phoenix mission (Pike et al. 2011). They revealed sorted dark grey basaltic sub-rounded to rounded fine sand particles due to wind saltation, with diameter between 80 and 200  $\mu\text{m}$ , as seen in Figure 9 from the Phoenix mission (Goetz et al. 2010). This range is compatible with the average diameter (170  $\mu\text{m}$ ) derived from thermal inertia measured at the InSight landing site. Bright red dust particles (2 – 5  $\mu\text{m}$ ) of slightly chemically altered basalt are also observed (Arvidson et al. 2004a, b, Golombek et al. 2006a, b and Goetz et al. 2010).

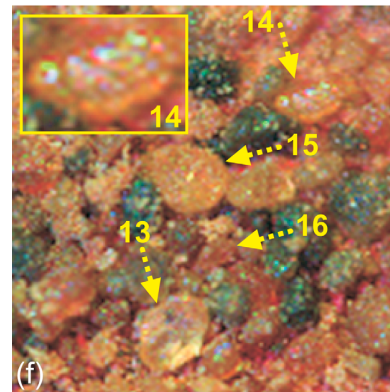


Figure 9. Microscopic observation of sub-rounded to rounded particles of Mars regolith at the Phoenix site. Picture width is 500  $\mu\text{m}$  (Goetz et al. 2010).

The colour of the particles in Figure 9 varies from dark gray (black) to slightly reddish. This probably depends on the degree of contamination of their surface by red fines, or on surface stains (Goetz et al. 2010).

Figure 10 shows the walls formed during the excavation of the surface by the rocket exhaust beneath the lander. It provides more evidence of the nature of the regolith, confirmed afterwards by observing the pit created around the mole during hammering.

At meter scale, the nature of the surficial regolith is spatially heterogeneous within the Homestead Hollow. ~10 cm-deep pits show ~centimeter-size pebbles embedded in a finer grain matrix which maintains a steep slope, suggesting some degree of cohesion. The slopes of regolith material piled at the bottom of the excavation particles moved by the rocket exhaust are also observed.

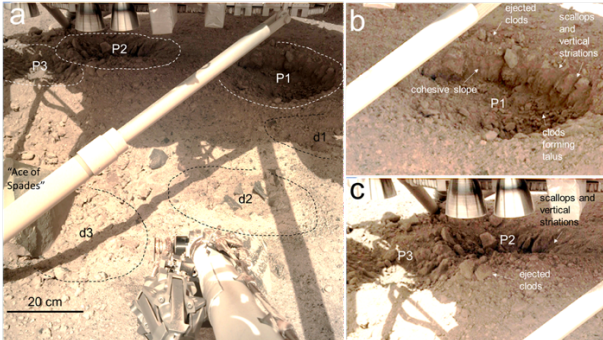


Figure 10. IDC images taken beneath the lander on sol 18. (a) The pits and depressions were excavated by the lander’s retrorockets. P1 and P2 are the largest and deepest pits. (b) P1 is ~50 cm in diameter and reveals ~12 cm of the shallow stratigraphy. The pit walls are vertically striated and steep (up to 65°) and expose an up to ~10-cm-thick cohesive duricrust comprised of weakly cohesive fine sand. The floor of each pit contains abundant reddish, pebble-size clasts or clods of material that broke off the steep pit walls. Dark-gray pebbles of likely basaltic composition are visible within the matrix of fine sand (Warner et al. 2022).

Further observation of the near-surface has been made possible by the pit that developed around the mole, observable once the support structure was removed by the IDA.



Figure 11. Image of the hole created by the HP3 mole during hammering (inclined ~15°), with the scoop appearing on top right (image credit JPL/NASA).

The photo of Figure 11 shows the pit created around the inclined mole (inclined 15°), with an almost vertical wall made up of resistant layers containing some pebbles. The steep edge and some overhangs indicate the existence of cohesion. Pebbles are embedded in a fine-grained matrix, indicating cementation.

Consistent with the formation process of the regolith (see Figure 6) and from observing the photos taken around the InSight landing site by the two cameras, Golombek et al. (2021) proposed the sketch of Figure 12 to describe the structure of the regolith in the landing area. A depression of ~27 m in diameter (in which the lander sits) interpreted as an ancient degraded and in-filled impact crater in the regolith is underlain by blocky ejecta and fractured basaltic bedrock. The crater has been filled dominantly by sand moved by the wind, producing an upper layer of fine material three meters thick, consisting mostly of sand.

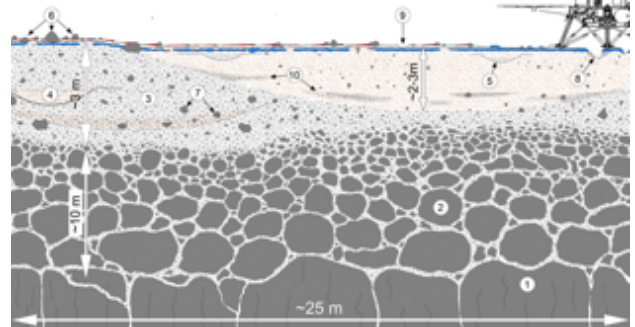


Figure 12. Interpretative cross-section of the shallow surface beneath the InSight lander (Golombek et al. 2020a, Creative Commons CC BY license). 1: Fractured basalt flow; 2: Blocky ejecta; 3: Fine-grained impact generated regolith; 4, 5: Overlapping craters; 6: Rockier area; 7: Rocks embedded in regolith; 8: Pits opened by retro rockets during landing; 9: Surface divots; 10: Lens of ejecta from other craters (Golombek et al. 2020a).

#### 4. SMALL STRAIN PROPERTIES OF THE SURFACE REGOLITH

The small strain investigation of the regolith mechanical properties presented below has been carried out either by wave velocity measurements or by small strain plate loading, with quite reversible responses. As a consequence, one considers that they reasonably provide some elastic parameters of the regolith, that will be considered here isotropic and homogeneous, for sake of simplicity.

##### 4.1. Previous estimation from lab tests

Some first estimations of possible elastic values of the Mars regolith were derived from wave velocity measurements carried out on Earth for Mars regolith simulants provided by both NASA (Mojave sand) and DLR (MSS-D and Eifelsand). In a standard fashion, wave velocities were measured by using piezo-ceramic bender elements on triaxial samples (100 mm in diameter and 200 mm in height), yielding the change in velocities with confining pressure shown in Figure 13a (Delage et al. 2017) for compression waves ( $V_p$ ) in the Mojave simulant.

A power law fit corresponding to the following expression of the changes in wave velocity with stress (see Santamarina et al. 2001) is drawn in Figure 13a:

$$V = \alpha \left( \frac{\sigma'_0}{1 \text{ kPa}} \right)^\beta \quad (2)$$

From this fit, a value  $\beta=0.3$  can be deduced. Note that, given the angular nature of the simulants investigated, this value might be somewhat overestimated. For rounded/subrounded grains like those observed on Mars, a value of 0.28 could be more appropriate. Figure 13b shows a linear relation between  $V_p$  and  $V_s$  for all three simulants, according to the following relation, in which  $\nu$  is the Poisson’s ratio:

$$\frac{V_p}{V_s} = \sqrt{\frac{2(1-\nu)}{1-2\nu}} \quad (3)$$

A common value  $\nu=0.22$  is derived for the three simulants from these data, at densities around 1.5 Mg/m<sup>3</sup>.

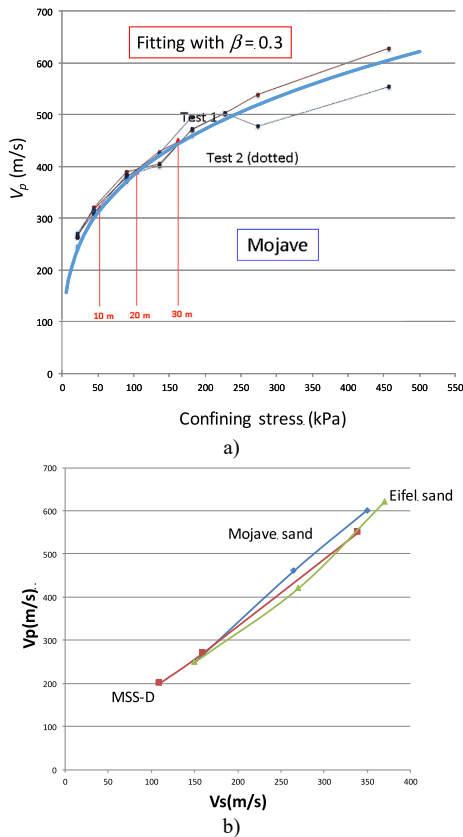


Figure 13. Bender elements measurements of velocity waves: a) changes in  $V_p$  with confining stress; b) linear relation between  $V_p$  and  $V_s$  for the three simulants investigated. A common value  $\nu = 0.22$  is obtained for the three simulants tested (Delage et al. 2017).

Further lab investigations, carried out to investigate the SEIS/regolith elastic interaction, also provide some information on possible elastic properties at the surface (Delage et al. 2022). This interaction was experimentally examined by using the device presented in Figure 15, in which a model of the SEIS foot (that consists of a 60 mm diameter disk with a 20 mm long spike in its center, see Figure 14), is slowly penetrated into a loose sand mass (unit mass around  $1.4 \text{ Mg/m}^3$ ) contained in a 240 mm diameter and 120 mm depth container. These tests were carried out on samples made up of a new rounded/subrounded simulant, the Fontainebleau sand. This sand is well-sorted, with an average diameter of  $220 \mu\text{m}$ , slightly larger than the average estimated size of  $170 \mu\text{m}$  on Mars derived from thermal inertia measurements.

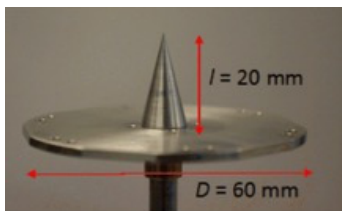


Figure 14. Shape of the SEIS foot (Delage et al. 2022). The conical spike has a maximum diameter of 10 mm.

As seen in Figure 15, the container is placed on the plate of a triaxial press that is slowly moved upwards ( $0.08 \text{ mm/min}$ ) so as to cause the penetration of the foot (spike + disk) that is fixed to the top of press through a sensitive force transducer that provides the change in penetration force while the plate is moved upwards. The maximum applicable load is defined by the weight of the suspended foot, that is equal to 10 N, i.e., the force supported by one of the three SEIS foot under Mars gravity. Special

care was taken during the setting up of this experiment to ensure sufficient stiffness of the device, as well as satisfactory thermal insulation (not shown in the Figure) to get satisfactory precision in displacement measurements. Displacements were measured by using high precision LVDT sensors.

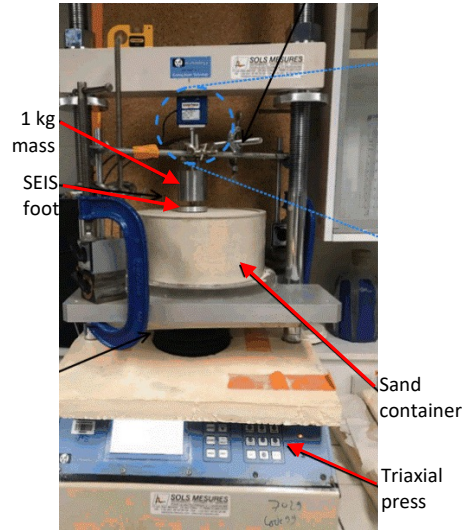


Figure 15. Experimental investigation of the interaction between the SEIS foot and a loose sample of Fontainebleau sand. The container is slowly moved upwards to cause penetration of the foot (Delage et al. 2022).

Figure 16 shows 10 force/displacement curves obtained on various samples of around  $1.4 \text{ Mg/m}^3$  unit mass. Note that a comparison between plate loading tests (with disk only) and foot loading tests (with disk and spike) didn't show any significant effect of the spike. A first series of curves exhibit a maximum penetration of around  $450 \mu\text{m}$  under the maximum force of 10 N, whereas a second series displays a maximum penetration of  $600 \mu\text{m}$ . These variations are linked to possible changes in the density at surface of the sample. When compared to the average grain size ( $220 \mu\text{m}$ ), the penetration under the maximum force corresponds to the size of two to three grains only, showing quite a small strain level.

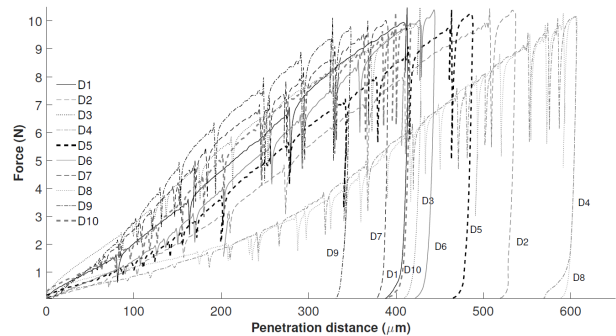


Figure 16. Force/displacement curves of the foot penetration tests (Delage et al. 2022).

The curves also exhibit some sudden repeated drops in forces followed by force recovery paths that return the curves to the same levels of force, that are related to stick-slips phenomena between the foot and the loose sand.

The interpretation of these data was made by using Sneddon's (1946) elastic solution of plate loading on a homogeneous semi-infinite half mass. This provides the following simple relation between the Young modulus  $E$ , the Poisson ratio  $\nu$ , the spring constant  $k_v$  and the plate radius  $R$ :

$$E = \frac{k_v(1 - \nu^2)}{2R} \quad (4)$$

The spring constant  $k_v = 1.47 \times 10^6$  N/m was deduced from the slope of force cycles carried out around the maximum force, as shown in Figure 17. Note that the cycle mobilizes a small displacement of  $1.5 \mu\text{m}$ , to be compared to the average grain size of  $220 \mu\text{m}$ , ensuring a fairly reversible response, as observed in Figure 7.  $k_v$  values were used to investigate the dynamic interaction between the SEIS and the ground (Fayon et al. 2018).

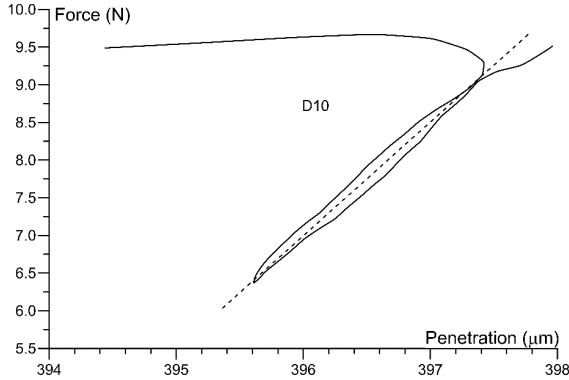


Figure 17. Force cycle performed around the maximum force corresponding to the force supported by a SEIS foot. The cycle is fairly reversible illustrating satisfactory elastic response under the imposed displacement (around  $2 \mu\text{m}$ ). Its slope provides the elastic spring constant  $k_v$  used in the analysis of the dynamic interaction between SEIS and the ground (Delage et al. 2022)

By considering an average response of the various tests performed, an average value of 20 MPa was deduced for the Young modulus. This value is typical of loose sand on the Earth. Based on relation (5) with  $\nu = 0.22$  and  $\rho = 1.4 \text{ Mg/m}^3$ , a value  $V_p = 128 \text{ m/s}$  is obtained, not far from those measured at the InSight site (Lognonné et al. 2020, Brinkman et al. 2022, see below).

$$V_p = \sqrt{\frac{E(1-\nu)}{\rho(1+\nu)(1-2\nu)}} \quad (5)$$

It is clear however that terrestrial lab experiments can only provide a magnitude estimate of the elastic properties of the regolith, given the possible differences in density, homogeneity, grain size distribution and shape (see Figure 10 and Figure 11) and gravity with the actual state of the regolith at the InSight site, which is discussed in the next session.

## 4.2. Direct estimation from Mars data

### 4.2.1. SEIS-HP<sup>3</sup> interaction

As seen in Figure 18, the SEIS was placed at a distance of around 1.18 m from HP<sup>3</sup>. Recording the HP<sup>3</sup> mole hammering noise with SEIS provided a unique opportunity to estimate the seismic velocities of the shallowest regolith *in situ* (Kedar et al. 2017; Sollberger et al. 2021; Brinkman et al. 2022). Brinkman et al. (2022) determined effective *P*- and *S*-wave velocities of  $V_p = 114_{-20}^{+43} \text{ m/s}$  and  $V_s = 60_{-7}^{+11} \text{ m/s}$  respectively, from around 2,000 HP<sup>3</sup> hammer stroke recordings. These seismic velocities likely represent bulk values for the uppermost several 10's of cm of regolith. The incidence angles of the *P*-wave first-arrivals provided an independent  $V_p/V_s$  ratio estimate of  $1.84_{-0.35}^{+0.89}$ , which is in good agreement with the travel-time based estimate of  $1.92_{-0.28}^{+0.52}$ .

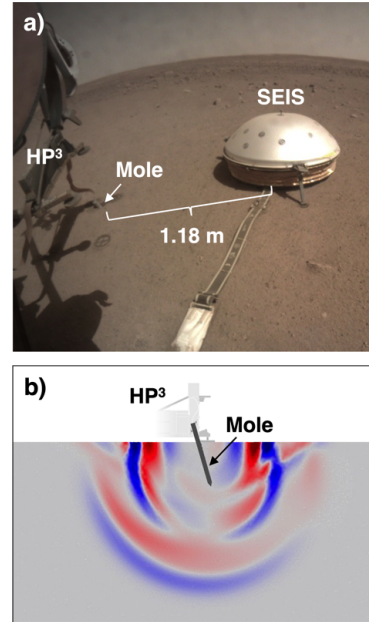


Figure 18. a) Image taken on June 28, 2019 (sol 209) showing how the HP<sup>3</sup> support structure was lifted and revealing the partially buried mole (see Figure 11), located around 1.18 m away from InSight's seismometer SEIS (image credit JPL/NASA); b) Conceptual illustration of the HP<sup>3</sup> mole generating seismic waves (blue and red colors correspond to negative and positive amplitudes) propagating through the shallow subsurface at the InSight landing site (Brinkman et al. 2022).

Assuming a density of  $1.2 \text{ Mg/m}^3$  (Spohn et al. 2021a), the  $V_p$  and  $V_s$  estimates can be converted into a bulk, shear, and Young's modulus of  $9.8 \pm 6.8 \text{ MPa}$ ,  $4.3 \pm 1.0 \text{ MPa}$ ,  $11.3 \pm 2.9 \text{ MPa}$ , respectively, and a Poisson's ratio of  $0.31 \pm 0.15$  (actually larger than that derived for lab measurements equal to 0.22). When interpreting these numbers, one has to keep in mind that they represent values for a homogeneous half-space and were derived from seismic waves with a dominant frequency of around 60 Hz.

### 4.2.2. Thermal effects

The observation of the Phobos transits by the different sensors on InSight led to an unexpected soil mechanics experiment (Stähler et al. 2020). The largest observed Phobos transit on 05/03/2019 lasted 27 seconds and led to a peak drop in solar array current of 10%. While no visual observation of the Sun was made during the transit, we can take the drop in solar array current as a proxy for the fraction of the solar disc covered at the peak of the transit, and that is consistent with simulations of the transit as depicted in Figure 19a, that shows how the solar disk is hidden by Phobos on sol 96 (3 March 2019). A complementary observation comes from the radiometer on board the lander. It provides a direct observation of the cooling of the Martian surface during the transit by  $1.3^\circ\text{K}$ . The skin depth of such a short negative heat pulse is only 0.5-1.0 mm. Thermal modeling of the temperature response indicates that the equivalent thermal inertia in this layer is only  $103 \text{ J m}^{-2}\text{K}^{-1}\text{s}^{-1/2}$ , significantly lower than that of the diurnal skin depth (Mueller et al. 2021). The atmospheric sensors measuring wind and air pressure did not record a detectable response to the transit while the magnetometer located under the deck of the lander recorded a drop in the magnetic field components completely in phase with the drop in the solar array currents. These magnetometer signals can be fully explained by the array currents and do not indicate any variations of the ambient magnetic field.

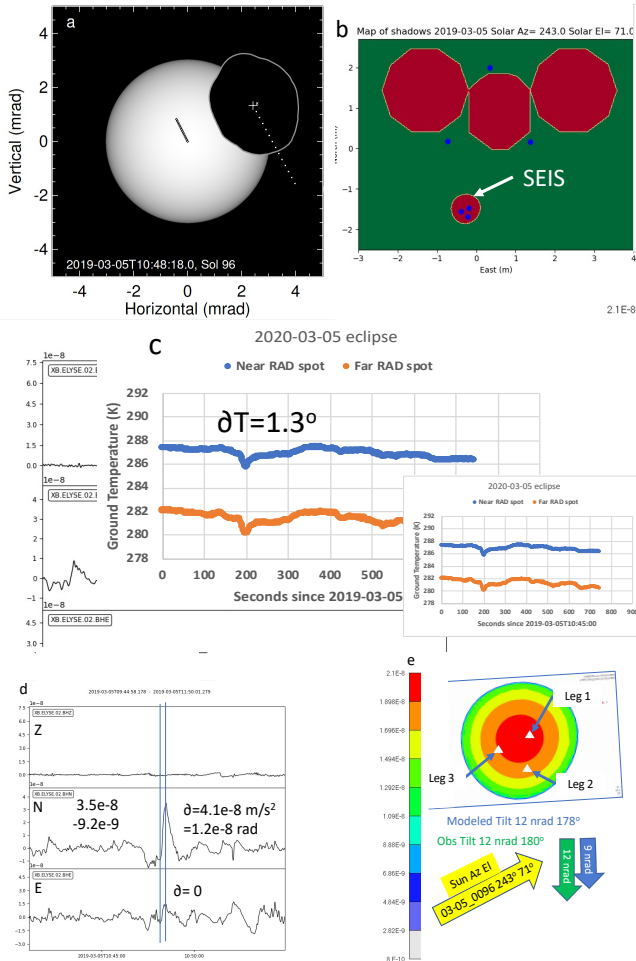


Figure 19. a) Simulated view of the transit of Phobos at maximum on 3rd March 2019, showing how the solar disk is partially hidden by Phobos. The dots to the right of the Phobos center of mass (+) are its position at 1-sec intervals preceding the timestamp; the diamonds to the left of the Sun center of mass are its position at 1-sec intervals preceding the timestamp; b) Projected shadows of the lander and the SEIS Wind and Thermal Shield. Blue dots are the locations of the Lander feet and the SEIS feet. c) Ground temperature as measured by the HP<sup>3</sup> RAD radiometer. d) Acceleration time series measured by SEIS along vertical (Z), north (N) and east (E). e) FEM model output of vertical motions at the seismometer.

From the above information, one might expect that the VBB seismometer, which is installed directly on the Martian surface and is covered by multiple thermal shields, should not respond to a Phobos transit, particularly because the thermal time constant between the ambient air temperature and the VBB core sensor temperature is in excess of 8 hours. However, this is not what happened. In fact, what we observe with high signal-to-noise ratio is that the VBB detects a purely horizontal acceleration toward the north. Interpreted as a tilt, we observe a downward tilting to the south by 12 nrad, that are correctly predicted by FEM calculations, as seen in Figure 19. The onset of this response is delayed relative to the solar array currents by ~5 seconds. If it weren't for this time delay, one could have speculated that some electric cross talk as in the case of the magnetometer might be responsible for the VBB signal. However, a subsequently performed experiment with an equally well shielded seismometer at the Black Forest Observatory in Germany, that simulated the radiation time history of the Phobos transit, showed that also the terrestrial seismometer responded with a purely horizontal acceleration, but with a 12s delay relative to the radiation onset.

With subsequent thermoelastic finite element modeling we established that thermoelastic strains caused by cooling of the top 0.5-1.0 mm of regolith everywhere except the area shadowed by the WTS dome can explain the observed tilting of the seismometer. The very thin (skin depth: 0.5-1mm) top layer of the regolith is elastically coupled to the material below and as soon as the top layer contracts, the medium below must follow elastically. Stähler et al. (2020) invoked local inhomogeneities in the regolith to convert the nearly uniform strain field into tilts. Since the Stähler et al. (2020) paper, we found that the tilts can also be modeled by a regolith with a more rigid top layer of 15-25 cm thickness. This is consistent with other observations of a more cohesive duricrust layer seen in the pits under the lander descent engines and around the HP<sup>3</sup> mole. (Figure 10 and Figure 11, Spohn et al. 2021, Golombek et al. 2020a).

This three-layer solution is, at the moment, non-unique and there is therefore large uncertainty in the duricrust thickness and the rigidity contrast between it and the material below. The range of parameters that can fit the data by trading off against each other is given in Table 2. Glitches in the seismometer data (see Kim et al 2021) likely caused by thermoelastic stick-slip events within the instrument complicate the extraction of the tilts. We hope to be able to constrain these parameters better with additional data from future Phobos transits. It is worthy of note that the Lander shadow does not contribute to the tilt at the seismometer. Tilts are confined to within the shadow in which they are generated and measured. It is fortuitous that the seismometer is deliberately offset from the center of the WTS dome, and that the shadow is slightly asymmetric due to the sun not being directly overhead. If the geometry were fully symmetric and the duricrust homogeneous, there would be no tilts to observe at the seismometer.

Table 2. The parameters of the thermoelastic model.

Top skin thickness	0.5 mm
Skin temperature change	Depends on which transit
Duricrust thickness	15 to 25 cm
$G_{\text{DURICRUST}}/G_{\text{HALFSPACE}}$	1.5 to 2.2
Poisson Ratio	-0.1 to 0.25
Thermal Expansion	$6.9 \times 10^{-6}$ to $1.0 \times 10^{-5}$ per K

#### 4.2.3. Convective vortices

Convective vortices (named dust devils when the vortex transports dust particles) are detected as a sharp dip in local pressure in the time series (e.g., Murphy et al. 2016). The day time turbulence at the InSight landing site is very active, leading to a vast population of 6000 recorded convective vortex encounters over the first 400 sols of operations (Banfield et al. 2020; Spiga et al. 2020). During its passage, the relatively low atmospheric pressure at the center of a convective vortex pulls the elastic ground up causing the surface to tilt away from the vortex. This leads to a tilt signature on the horizontal component of a seismometer in contact with the ground. The isolated seismic signature of a convective vortex was first detected on Earth in 2015 (Lorenz et al. 2015) and has since been detected on Mars with SEIS (Lognonné et al. 2020; Banerdt et al. 2020), including at high frequencies (Lorenz et al., 2021).

In the context of the InSight mission, vortex modelling of the seismic and pressure data has contributed to providing the first constraints on the average properties of the shallow elastic structure of Mars (Lognonné et al. 2020). These initial analyses used the plane wave approach of Sorrells' theory (Kenda et al. 2020), that is based on elastic calculations of the effects of change in gas pressure at the surface of a semi-infinite layered half-space. The point-source modelling approach has also been used to interpret joint observations of a dust devil vortex made by orbital imaging,

in-situ imaging, SEIS and the InSight pressure and wind sensors (Banerdt et al. 2020). Through waveform fitting, the simple vortex model allowed the dust devil pressure drop event to be identified among the multiple pressure drops present in the data. The Young's modulus of the upper few meters of the Martian subsurface in a specific known location at a distance of ~20 m from the lander was then determined to be ~270 MPa by combining the information from the multiple instruments (Banerdt et al. 2020). More recent analyses (Onodera, 2022) have been made on more than 500 pressure drops and for different wind levels. This allows a better resolution with depth in the ground rigidity determination, as wind and period are the two key parameters enabling the control of the depth sensitivity of the compliance method. This confirms the gradient with depth of previous studies and shows that the first upper meter below SEIS is made with material of about 20 MPa, while deeper, the Young's modulus rises from 300-500 MPa at a few meters to 500-800 MPa deeper than 50 m.

In another analyses studying almost 500 vortices, Murdoch et al. (2021) estimate that the mean value of  $\eta$  ( $\eta = E/[1 - \nu^2]$ , where  $E$  is the Young's modulus and  $\nu$  is the Poisson's ratio) of the Martian ground in the region around SEIS is 239 +/- 140 MPa from seismic and pressure data filtered in the (0.02 – 0.3 Hz) frequency band. These average elastic properties are similar to those found in studies focusing on compliance analysis mentioned previously (Garcia et al. 2020; Kenda et al. 2020; Lognonné et al. 2020). These values, significantly larger than those determined at the first centimeters by in-situ wave velocity measurements or preliminary lab tests on Earth, correspond to a larger depth and integrate the effects of the blocky ejecta illustrated in Figure 12 below 12 m.

By studying the direction of the ground tilt at the closest approach (when radial tilt amplitude is largest), it would appear that the majority of seismically detected dust devils have a closest approach to the east of SEIS and that there is a distinct lack of detections to the west (Golombek et al. 2020c). However, the vortices that lift dust also leave behind tracks on the surface of Mars that are visible from satellites in orbit. Perrin et al. (2020) use post-landing high-resolution satellite images to monitor dust devil activity during the first eight months of the mission. They find that the dust devil tracks observed around the InSight landing site from orbit indicate a preferential direction, aligned closely with the most common wind direction (~N145°E +/- 30°), but are not preferentially located to the east of SEIS. Murdoch et al. (2021) demonstrate that a plausible explanation for the observed close-approach azimuth bias in the seismic data is that the ground is softer to the east thus increasing the number of seismic detections of vortices on that side. Such an interpretation of 'softer' ground to the east is consistent with geomorphological surface interpretations (Golombek et al. 2020).

## 5. FAILURE PROPERTIES

Soil mechanics experiments aiming at characterizing the mechanical failure properties (i.e., the internal friction angle and the cohesion) have been performed using the IDA. Specifically, the IDA and its scoop (see Figure 8) were used around sol 673 (i.e., the 673<sup>rd</sup> day of the mission) to apply pressure on the ground near HP<sup>3</sup>, as well as scrape, scoop, and dump the loose surface material (Marteau et al. 2021). They also have been more recently used to bury the SEIS tether (from sol 802), in an attempt to get an improved thermal insulation of the tether from the atmospheric temperature changes (~100°C from day to night), respectively), so as to reduce the glitches and noise affecting the SEIS seismological data. Observation of scrapes, trenches and dumped piles provided interesting information on the mechanical properties of the regolith at the InSight site.

### 5.1. IDA pressing over the mole pit

Shear strength parameters for the regolith at the mole pit have been estimated by a back-analysis of the observed geometry at the pit wall during soil loading by the lander's robotic arm scoop (Marteau et al. 2021). Depending on the orientation of the scoop, two different pushes were applied on the regolith: a flat push (see Figure 8) and a tip push. The width and depth of the hole were set equal to 0.045 m and 0.07 m, respectively, with a wall inclination equal to 85° (see the shape of the pit in Figure 11).

For the analysis, a 3D finite element model has been employed, assuming an elasto-plastic Mohr-Coulomb failure criterion for the material. Soil unit weight soil in the Mars environment was set equal to 4.526 kN/m<sup>3</sup> (corresponding to a unit mass of 1.216 Mg/m<sup>3</sup> under Mars gravity of 3,721 m/s<sup>2</sup>). A friction angle of  $\phi = 30^\circ$  was fixed for all calculations and the required cohesion was determined iteratively so that the stability criterion is just fulfilled, with a safety factor  $\eta = 1$ .

The applied force of 29 N derived from the motor currents activating the IDA for the flat push was distributed over a square footprint area (side length = 0.07 m) corresponding to the scoop width (Figure 8), with a trapezoidal intensity starting with zero along the front line, attaining a maximum of 7.89 kPa at the centre and remaining constant afterwards. For the tip push, the measured force of 45 N has been converted to a rectangular load of intensity 91.84 kPa distributed over a footprint area of 0.07 m by 0.007 m. The inferred minimum cohesion values are  $c' = 0.38$  kPa for the flat push and 5.8 kPa for the tip push. Figure 20 displays the model with displacement contours for the flat push.

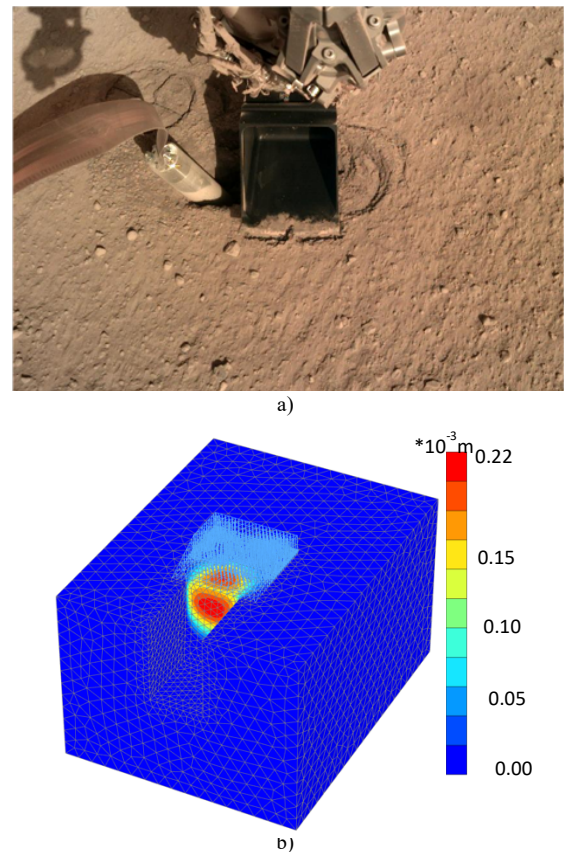


Figure 20. a) Photo of the scoop pressing above the pit; b) Finite element model with incremental displacement contours for the flat push (Vrettos 2022, pers. comm.).

5.2. Scraping and piling operations

During scraping operations, it is important to remind that the Martian soil is defined by three successive and different unit masses: i) the intact and densest one, prior to scraping; ii) the unit mass once extracted in the scoop, related to the previous one by an expansion ratio, estimated for sands on the Earth around 10% and iii) once dumped into a pile. In this case, it was observed, at least during the tether burial operations described below, that some proportions of finer particles were blown by the wind away from the pile. In other words, the material of the pile is somewhat coarser than that contained in the scoop. Investigations are presently carried out (Verdier et al. 2022) to estimate the proportion of fines submitted to the combined horizontal action of the wind (Stokes law, based on the wind speed and direction monitored by the weather station of the lander) and gravity, based on the photo identification of the surface along which these particles have been blown away.

On sol 673, two overlapping 12-cm long scrapes were commanded to bring regolith from the far side of the HP<sup>3</sup> pit towards the lander (Marteau et al. 2022). The scrapes created two piles near the HP<sup>3</sup> mole by bulldozing mounds of particles. From the elevation profiles extracted from the sol 673 digital elevation model (see Figure 21), one observes that the slopes of the bulldozed mounds of regolith can be as high as 38-39° on the upstream side (S1), where the particles have been pushed by the scoop. Once the scoop is no longer in contact with the regolith, particles likely cascade down the slope. On the downstream side, the slopes of the piles are between 49 to 53°. The walls formed by the sides (S2) of the scoop have steep slopes with values of 78° and 70°.

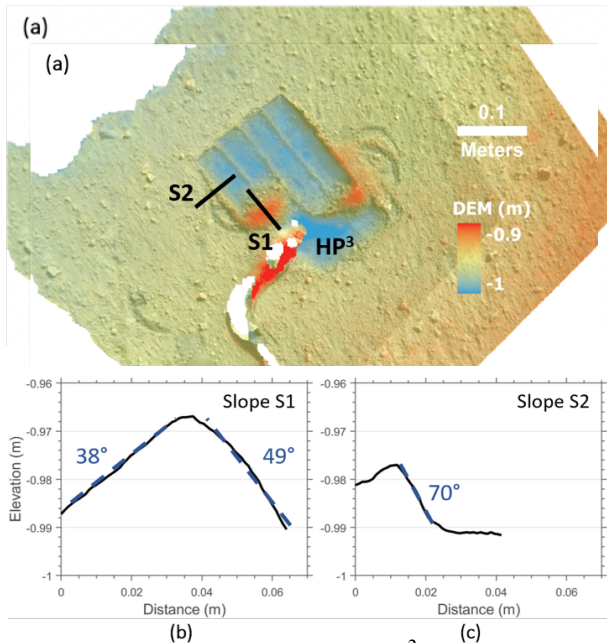


Figure 21. (a) Digital elevation model of the HP<sup>3</sup> pit based on the stereo pair taken on Sol 673 after scraping; (b) Elevation profile S1 of the scraped pile (c) Elevation profile S2 of the scraped wall (Marteau et al. 2022, Spohn et al. 2021a).

Starting on sol 803, the arm and scoop were used to bury the SEIS tether by creating a large number of scrapes, scooping and dumping the scraped regolith. The arm scraping activities created several scrapes from which the regolith was extracted (like in Figure 21). The regolith extracted in the scoop was then dumped in piles above the tether close to SEIS along line S2 in Figure 22, with some proportion blown away by the wind, as commented previously.

Elevation profiles were obtained from digital elevation models acquired between Sols 803 and 822 to measure the slopes of the scraped piles and walls. The average slope of the regolith mounds is between  $42^\circ \pm 2.7^\circ$  (with a range from  $40^\circ$  to  $45.8^\circ$ ), comparable to what is observed along line S1 in Figure 21. The side walls scraped by the vertical sides of the scoop have a slope value of  $54.7^\circ \pm 6.6^\circ$  (with a range from  $46^\circ$  to  $63^\circ$ ) smaller than those determined in Figure 21.

Subsequently, the IDA scooped and dumped the scraped material from a height of 40 cm on top of the SEIS tether. The digital elevation model and elevation profiles of the dumped pile obtained on Sol 877 are presented in Figure 22. At its highest point, the dumped pile is ~3 cm high and the material rests at slope value of  $24.1^\circ \pm 6.1^\circ$  (with a range from  $16.6^\circ$  to  $32^\circ$ ).

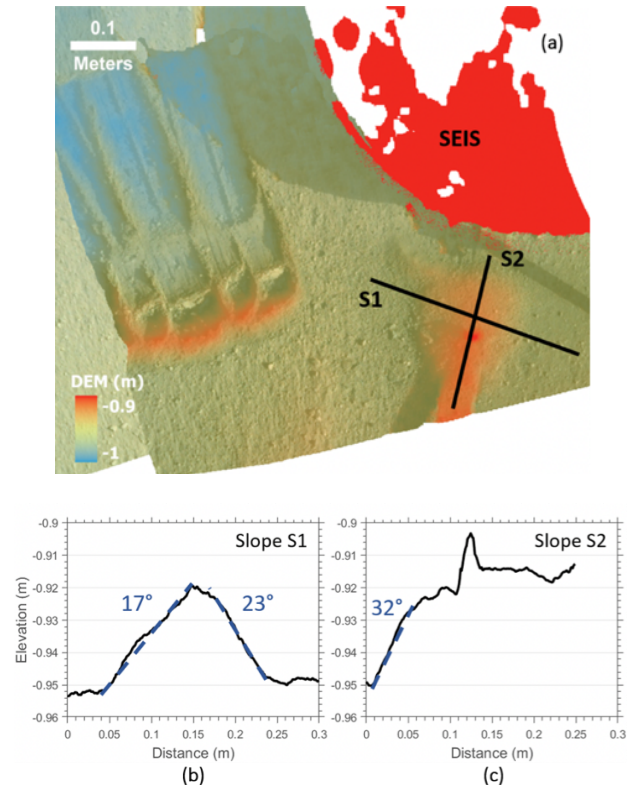


Figure 22. (a) Digital Elevation Model of the surface between HP<sup>3</sup> and SEIS based on the stereo pair taken on Sol 877 after scraping, scooping and dumping; (b) Elevation profile S1 of the dumped pile; (c) Elevation profile S2 of the dumped pile (Marteau et al. 2022).

The difference in slope angle between the dumped and scraped piles is first due to the difference between the materials, with less fine particles in the dumped piles. In the intact state of the regolith, these fine particles, mixed to sand, are known to provide some degree of cohesion also increased by low gravity (Walton et al. 2007). This would explain that the imprints of the scoop in the unconsolidated sand layer, like rover tracks on other missions, are perfectly smooth (Golombek et al. 2020a). This small cohesion explains that the wall along slope S2 in Figure 21 have such a high angle compared to the angle of repose. Another possible reason explaining the differences in slopes is most likely linked to the methods used to create the piles. Piles produced by pouring a material (from which finer particles have been blown out by the wind) from a given height yield different bulk densities and geometries than piles generated by scraping. Larger densities are obtained with larger heights. The fall height from the scoop was here around 45 cm.

The average slope value of  $42^\circ$  obtained from the scraped piles is rather high with respect to the typical friction angle of a

loose sub-rounded/rounded granular regolith (estimated around  $30^\circ$  at undisturbed state, Golombek et al. 2008, Morgan et al. 2018). This high slope value could be related to i) a larger friction angle of a soil mass that has been moved into a denser state as a result of pushing and compacting during scraping and ii) the effects of cohesive forces acting in conjunction with the presence of fines within the sand grains under low gravity conditions (Walton et al. 2007) and low atmospheric pressure (see Bromwell's (1966) work in lunar conditions). In addition, the slopes of the side walls created by the scrapes are larger than those of the piles, whereas slope failure was not seen on these walls. This confirms the presence of some inter-grains bounding forces, mainly due to the fine fraction, that provide some cohesion to the undisturbed soil. Finally, the average slope value of  $24.1^\circ$  obtained for the dumped piles can be interpreted as a lower bound estimate of the angle of repose of the soil (with no fines) in a loose remolded state.

## 6. PENETRATION ISSUES

The HP<sup>3</sup> was designed to measure the temperature profile, a thermal conductivity profile and related physical properties down to a depth of 3 – 5 m. The temperatures would have been measured using sensors on a tether that a small penetrator (the mole) would have dragged down (Spohn et al. 2018). Upon penetration, a thermal conductivity and thermal diffusivity profile would have been measured using sensors embedded in the mole (e.g., Grott et al. 2021). From the product of the temperature gradient at a depth of at least 3 m and the thermal conductivity, the surface heat flow of Mars would have been calculated. It would have been required to reach that minimum depth to avoid the perturbation of the temperature gradient caused by seasonal variations of the surface temperature. The thermal conductivity and diffusivity measurements would have allowed an estimate of the density, and the mechanical strength of the soil would have been derived from the penetration rate that would have been recorded. Unfortunately, the mole did not penetrate deeper than a total of 40 cm. Therefore, the surface heat flow could not be determined, and the physical properties could only be derived down to that depth.

The mole was designed to penetrate cohesionless soil like quartz sand, which was expected to provide a good analogue material for Martian sand. The sand would provide friction to the buried mole hull to balance the remaining recoil of the mole hammer mechanism that drives the mole forward. Although a supressor mass and spring in the hammer mechanism absorbed much of the recoil, the available mass did not allow a system that would have eliminated the recoil altogether (Spohn et al. 2021b). The root cause of the failure - as was determined through an extensive, almost two years long campaign (Spohn et al. 2021a, b) - was a lack of friction in an unexpectedly thick cohesive and brittle duricrust. In addition, it was found that the Martian soil provided unexpected levels of penetration resistance. By precessing about a point midway along its hull, the mole carved a 7 cm deep and 5-6 cm wide pit during initial hammering and reached a depth of initially 31 cm aided by friction springs in the mole support structure.

During the campaign - described in detail in Spohn et al (2021a) - the mole penetrated further to a final depth of about 40 cm aided by friction applied using the scoop at the end of the IDA and by direct pressure by the latter. That brought the mole body 1 - 2 cm below the surface at which depth thermal conductivity measurements could be performed (Grott et al. 2021). The mole reversed its downward motion twice during attempts with the IDA to provide friction through pressure on the regolith instead of directly with the scoop to the hull.

The penetration record of the mole, the thermal conductivity and diffusivity measurements, and seismic data recorded during the hammerings were used to derive a model of the properties of the first 40 cm of the Martian soil at the landing site (Spohn et al. 2021a). Accordingly, a duricrust of about 20 cm thickness is found underneath a one-centimeter-thick unconsolidated sand and dust layer. Beneath the duricrust a sand layer of about ten-centimeter thickness is found followed by a layer of a sand mixed with gravel, possibly consisting of debris from a small impact crater.

The penetration resistance of the sand/gravel layer is best constrained and was found to be 5.3 MPa while the duricrust has a 5 to 10 times smaller penetration resistance. Applying cone penetration theory, the resistance of the duricrust was used to estimate its cohesion to be 4 - 25 kPa, depending on the assumed internal friction angle of the duricrust. Pushing the scoop with its blade into the surface and chopping off a piece of duricrust provided another estimate of the cohesion of about 6 kPa.

The density of the topmost sand layer is estimated to be  $1.3 \text{ Mg/m}^3$  while that of the duricrust is  $1.1 \text{ Mg/m}^3$ , followed by  $1.3 \text{ Mg/m}^3$  for the sand layer underneath and by  $1.6 \text{ Mg/m}^3$  for the sand/gravel layer. The thermal conductivity increases from  $14 \text{ mWm}^{-1}\text{K}^{-1}$  to  $34 \text{ mWm}^{-1}\text{K}^{-1}$  through the one-centimeter sand/dust layer, keeps the latter value in the duricrust and the sand layer underneath and then increases to  $64 \text{ mWm}^{-1}\text{K}^{-1}$  in the sand/gravel layer below (Grott et al. 2021).

## 7. CONCLUDING REMARKS

Increased interest in the physical and mechanical properties of the Martian soil started during the early Viking 1 and 2 missions (1976), which provided significant contributions from photos and trenching/scraping activities with their robotic arms. Many years later, the same approach has been adopted by the InSight mission and its IDA robotic arm. These data have been supported by better quality photos and, more importantly, completed by pioneering measurements of wave velocities at the surface of the planet during the hammering session of the HP<sup>3</sup> and the monitoring of their arrival by SEIS, providing valuable elastic parameters of the regolith at small strains. These parameters have been further constrained by compliance calculations allowed by the monitoring of the ground deformations induced by convective vortexes. Interestingly, previous estimates from through laboratory testing on Earth on regolith simulants provided good predictions of the parameters, including with respect to strength parameters. Of course, photo observations also demonstrated that the regolith on Mars is different from the simpler regolith simulants used in laboratory testing. Instead of being a well-sorted sand, it appears that it also contains some pebbles embedded in a sandy matrix with some degree of cohesion that might be partly related to the fine particles contained in the regolith, and also to the low gravity and atmospheric pressure conditions. Photo observations could also be completed by Digital Image modelling that provided accurate morphologies of the trenches and dumps made with the IDA scoop, both to support the attempts of mole penetration and the SEIS tether burying operations. The differences in slopes observed between trenches and piles were related to the way they were set up, evidencing some degree of cohesion due, among other things, to the fines contained in the sand/fine mixture. Interestingly, it was also observed that the fine fraction of the regolith was dispersed by the wind. This feature is presently analyzed to better constrain the proportion of fines contained in the surface regolith, which will provide interesting further information with respect to the previous estimation get by thermal inertia measurements.

Complementary information has also been gained from thermal measurements, that locally confirmed the preliminary orbiter thermal inertia measurements. In spite of the difficulties met by the mole, that could not be driven as planned, the (very low) thermal conductivity at surface could be directly determined by the HP<sup>3</sup> probe. Thermal changes and their thermo-elastic effects on the surface were also detected during Phobos eclipses, together with the effects of change in atmospheric pressure, thanks to the very high sensitivity of SEIS.

Further soil mechanics tests are now planned for the remaining of the mission, in which the robotic arm will be used to apply controlled forces on the ground, while measuring the resulting tilts by SEIS. In other words, this successful geophysical mission also provided – and will provide – significant geological and geotechnical results.

## 8. ACKNOWLEDGEMENTS

We acknowledge NASA, CNES, their partner agencies and Institutions (UKSA, SSO, DLR, JPL, IPGP-CNRS, ETHZ, IC, MPS-MPG) together with Ecole des Ponts ParisTech and Universidad de los Andes (Colombia) for supporting this work. This paper is InSight Contribution Number ICN 253.

## 9. REFERENCES

- Arvidson, R. E., et al. (2008), Spirit Mars Rover Mission to the Columbia Hills, Gusev crater: Mission overview and selected results from the Cumberland Ridge to Home Plate, *Journal of Geophysical Research: Planets*, 113, E12S33.
- Arvidson, R. E., et al. (2009), Results from the Mars Phoenix Lander Robotic Arm experiment, *Journal of Geophysical Research: Planets*, 114, E00E02.
- Banerdt, W.B., Smrekar, S.E., Banfield, D. et al. (2020). Initial results from the InSight mission on Mars. *Nature Geosciences* 13, 183–189.
- Banfield, D., Spiga, A., Newman, C. et al. (2020). The atmosphere of Mars as observed by InSight. *Nature Geosciences* 13, 190–198.
- Brinkman, N., Schmelzbach, C., Sollberger, D. et al (2022) In-situ regolith seismic velocity measurement at the InSight landing site on Mars. submitted to *Journal of Geophysical Research: Planets*
- Ferguson, R., Christensen, P., Bell, J., Golombek, M., Herkenhoff, K., & Kieffer, H. (2006). Physical properties of the Mars Exploration Rover landing sites as inferred from Mini-TES-derived thermal inertia. *Journal of Geophysical Research: Planets* 111(E2), E02S21.
- Bromwell, L. (1966). The friction of quartz in high vacuum. *Materials Science Report*, MIT, Cambridge Mass.
- Cantor, B.A., (2007). MOC observations of the 2001 Mars planet encircling dust storm. *Icarus* 186, 60–96.
- Christensen P.R., H.J. Moore (1992). The martian surface layer, in MARS, ed. by H.H. Kieffer, B.M. Jakosky, C.W. Snyder, M.S. Matthews (University of Arizona Press, Tucson, 1992), pp. 686–727
- Delage P., Karakostas F., Dhemaied A., Belmokhtar M., Lognonné P., Golombek M. et al. 2017. An investigation of the mechanical properties of some Martian regolith simulants with respect to the surface properties at the InSight mission landing site. *Space Science Reviews*, 211, 191-213
- Delage P., Castillo-Betancourt J.P., Caicedo-Hormaza B., Karakostas F., De Laure E., Lognonné P., Antonangeli D., Banerdt B. (2022). The interaction between the SEIS seismometer of the InSight Martian mission and a regolith simulant. *Géotechnique*, accepted.
- Edwards, C. S., Piqueux, S., Hamilton, V. E., Ferguson, R. L., Herkenhoff, K. E., Vasavada, A. R., et al. (2018). The thermophysical properties of the Bagnold dunes, Mars: Ground-truthing orbital data. *Journal of Geophysical Research: Planets*, 123, 1307– 1326.
- Fayon L., Knapmeyer-Endrun B., Lognonné P., Bierwirth P., Kramer A., Delage P., Karakostas F. et al. (2018). A numerical model of the SEIS leveling system transfer matrix and resonances: application to SEIS rotational seismology and dynamic ground interaction. *Space Science Reviews*, 214: 119.
- Folkner, W. M., Dehant V., Le Maistre S., Yseboodt M., Rivoldini A. et al. (2018). The rotation and interior structure experiment on the InSight mission to Mars. *Space Science Reviews* 214, 100.
- Garcia, R. F., Kenda, B., Kawamura, T., Spiga, A., Murdoch, N., Lognonné, P. H., et al. (2020). Pressure effects on the SEIS-InSight instrument, improvement of seismic records, and characterization of long period atmospheric waves from ground displacements. *Journal of Geophysical Research: Planets*, 125, e2019JE006278.
- Giardini D., Lognonné P., Baerdt W.P., Pike W.T., Christensen et al. (2020). The seismicity of Mars. *Nature Geosciences* 13, pages 205–212.
- Goetz W. et al., Microscopy analysis of soils at the Phoenix landing site, Mars: classification of soil particles and description of their optical and magnetic properties. *Journal of Geophysical Research: Planets* 115, E00E22 (2010).
- Golombek, M., Haldemann, A. F. C., Simpson, R. A., Ferguson, R. L., et al. (2008). Martian surface properties from joint analysis of orbital, Earth-based, and surface observations. In I. Bell Jim (Ed.), *The Martian surface composition, mineralogy, and physical properties* (Ch. 8).
- Golombek, M., Kipp D., Warner I.J., Daubar I.J., Ferguson R.L., Kirk R.L. et al. (2017). Selection of the InSight landing site. *Space Science Review* 211, 5–95.
- Golombek M., · M. Grott, · G. Kargl, · J. Andrade, · J. Marshall, · N. Warner, · N.A. Teanby, · V. Ansan et al. (2018). Geology and Physical Properties Investigations by the InSight Lander. *Space Science Review* 214:84.
- Golombek, M., Warner, N. H., Grant, J. A., Hauber, E., et al., (2020)a, Geology of the InSight landing site on Mars: *Nature Communications*, 11, 1014.
- Golombek, M., Kass, D., Williams, N., Warner, N., Daubar, I., Piqueux, S., Charalambous, C., and Pike, W. T., (2020)b, Assessment of InSight landing site predictions: *Journal of Geophysical Research: Planets*, v. 125, e2020JE006502.
- Golombek, M., Williams, N., Warner, N. H., et al, (2020)c, Location and setting of the Mars InSight lander, instruments and landing site, *Earth and Space Science*, v. 7, e2020EA001248.
- Golombek, M., Charalambous, C., Pike, W. T., and Sullivan, R., (2020)d, The origin of sand and dust on Mars: Evidence from the InSight landing site: *51<sup>st</sup> Lunar and Planetary Science Conference*, Abstract #2744, Lunar and Planetary Institute, Houston.
- Grott, M., Spohn, T., Knollenberg, J., Krause, C., Scharringhausen, M., Wippermann, T., et al. (2019). Calibration of the heat flow and physical properties package (HP<sup>3</sup>) for the InSight Mars mission. *Earth and Space Science*, 6(12), 2556–2574.
- Grott, M., T. Spohn, J. Knollenberg et al. (2021) Thermal conductivity of the Martian soil at the InSight landing site from HP3 active heating experiments. *Journal of Geophysical Research: Planets*, doi:10.1029/2021JE006861
- Hamilton, V. E., Vasavada, A. R., Sebastián, E., Torre Juárez, M., Ramos, M., Armiens, C., et al. (2014). Observations and preliminary science results from the first 100 sols of MSL Rover Environmental Monitoring Station ground temperature sensor measurements at Gale Crater. *Journal of Geophysical Research: Planets*, 119(4), 745–770.
- Herkenhoff, K. E., Golombek, M. P., Guinness, E. A., Johnson, J. B., Kusack, A., Richter, L., Sullivan, R. J., and Gorevan, S. (2008). In situ observations of the physical properties of the martian surface: Chapter 20 in *The Martian Surface: Composition, Mineralogy and Physical Properties*, J. F. Bell III editor, Cambridge University Press, p. 451-467.
- Kedar, S., Andrade, J., Banerdt, B., Delage, P., Golombek, M., Grott, M., et al. (2017). Analysis of regolith properties using seismic signals generated by InSights HP3 penetrator. *Space Science Reviews*, 211(1-4), 315–337.
- Kenda, B., Drilleau, M., Garcia, R. F., Kawamura, T., Murdoch, N., Compaire, N., et al. (2020). Subsurface structure at the InSight landing site from compliance measurements by seismic and meteorological experiments. *Journal of Geophysical Research: Planets*, 125, e2020JE006387.
- Kieffer, H. H., Martin, T. Z., Peterfreund, A. R., Jakosky, B. M., Miner, E. D., & Palluconi, F. D. (1977). Thermal and albedo mapping of Mars during the Viking primary mission. *Journal of Geophysical Research*, 82(B28), 4249–4291.
- Kim, D., Davis, P., Lekic, V., Maguire, R., Compaire, N., Schimmel, M., Stutzmann, E., Irving, J., Lognonné, P., Scholz, J-R., et al. (2021).

- Potential pitfalls in the analysis and structural interpretation of seismic data from the Mars InSight mission. *Bulletin of the Seismological Society of America*, 111 (6), 2982-3002.
- Lognonné P., W.B. Banerdt, D. Giardini, W.T. Pike, U. Christensen, P. Llaudet, S. de Raucourt et al. (2019). SEIS: InSight's Seismic Experiment for Internal Structure of Mars. *Space Science Review*, <https://doi.org/10.1007/s11214-018-0574-6>.
- Lognonné, P., W.B. Banerdt, W.T. Pike, et al. (2020). Constraints on the shallow elastic and anelastic structure of Mars from InSight seismic data, *Nature Geoscience*, <http://doi.org/10.1038/s41561-020-0536-y>.
- Lorenz, R. et al. (2015). Seismometer Detection of Dust Devil Vortices by Ground Tilt, *Bulletin of the Seismological Society of America*, 105(6): 3015.
- Lorenz, R.D. Spiga, A. Lognonné, P., Plasman, M., Newman, C.E., Charalambous, C. (2021). The whirlwinds of Elysium: A catalog and meteorological characteristics of "dust devil" vortices observed by InSight on Mars, *Icarus*, 355, doi : [10.1016/j.icarus.2020.114119](https://doi.org/10.1016/j.icarus.2020.114119).
- Marteau, E., Golombek, M., Vrettos, C., Garvin J. and Williams, N. (2021). Soil Mechanical Properties at the InSight Landing Site on Mars. *52nd Lunar and Planetary Science Conference (LPSC)*, Abstract #2067, Lunar and Planetary Institute, Houston
- Marteau E., M. Golombek, C. Vrettos, P. Delage, N.R. Williams, and V. Ansan (2022). Soil strength properties derived from scraping and dumping activities at the InSight landing site on Mars. *53rd Lunar and Planetary Science Conference*, Abstract 1253, Houston, USA.
- Mellon, M. T., Jakosky, B. M., Kieffer, H. H., & Christensen, P. R. (2000). High-resolution thermal inertia mapping from the Mars global surveyor thermal emission spectrometer. *Icarus*, 148(2), 437-455.
- Moore, H. J., G. D. Clow, and R. E. Hutton (1982). A summary of Viking sample-trench analyses for angles of internal friction and cohesions, *Journal of Geophysical Research: Planets* 87, 10043-50.
- Moore H.J., R.E. Hutton, G.D. Clow, and C.R. Spitzer (1987). Physical properties of the surface materials at the Viking landing sites on Mars. U.S. geological survey professional paper 1389.
- Moore, H. J., Jakosky, B. M. (1989). Viking landing sites, remote sensing observations, and physical properties of Martian surface materials. *Icarus* 81, 164 - 184.
- Morgan P., Grott M., Knapmeyer-Endrun B., Golombek M., Delage P., Lognonné P. et al. (2018). A pre-landing assessment of regolith properties at the InSight landing site, *Space Science Reviews* 214:104.
- Mueller, N. T., Knollenberg, J., Grott, M., Kopp, E., Walter, I., Krause, C., et al. (2020). Calibration of the HP<sup>3</sup> Radiometer on InSight. *Earth and Space Science*, 7(5), e01086.
- Mueller, N., S. Piqueux, M. Lemmon, J. Maki, R. D. Lorenz, M. Grott, et al. (2021). Near Surface Properties of Martian Regolith Derived From InSight HP<sup>3</sup>-RAD Temperature Observations During Phobos Transits. *Geophysical Research Letters* 48, e93542.
- Murdoch, N., Spiga, A., Lorenz, R., Garcia, R. F., Perrin, C., Widmer-Schmidrig, R., et al. (2021). Constraining Martian regolith and vortex parameters from combined seismic and meteorological measurements. *Journal of Geophysical Research: Planets*, 126, e2020JE006410.
- Murphy, J. et al., Field Measurements of Terrestrial and Martian Dust Devils. (2016) *Space Science Reviews*, vol. 203 (n° 1). pp. 39-87.
- Onodera, K. (2022). *Subsurface structure of the Moon and Mars deduced from 3D seismic wave propagation simulation and analysis of Apollo and InSight seismic data*, PhD Thesis, Université de Paris.
- Palluconi, F. D., & Kieffer, H. H. (1981). Thermal inertia mapping of Mars from 60°S to 60°N. *Icarus*, 45(2), 415-426.
- Pan, L., Quantin, C., Tauzin, B., Michaut, C., Golombek, M., Lognonné, P. et al. 2020, Crust stratigraphy and heterogeneities of the first kilometers at the dichotomy boundary in western Elysium Planitia and implications for InSight lander: *Icarus*, v. 338, 113511.
- Perrin, C., Rodriguez, S., Jacob, A., Lucas, A., Spiga, A., Murdoch, N., et al. (2020). Monitoring of dust devil tracks around the InSight landing site, Mars, and comparison with in situ atmospheric data. *Geophysical Research Letters*, 47, e2020GL087234.
- Piqueux, S., & Christensen, P. R. (2009). A model of thermal conductivity for planetary soils: 2. Theory for cemented soils. *Journal of Geophysical Research: Planets*, 114(E9), E09006.
- Piqueux, S., Mueller, N., Grott, M., Siegler, M., Millour, E., Forget, F., et al. (2021). Regolith Properties near the InSight Lander Derived from 50 Sols of Radiometer Measurements. *Journal of Geophysical Research: Planets*, submitted.
- Pou, L., Nimmo, F., Lognonné, P., Mimoun, D., Garcia, R. F., Pinot, B., A. Rivoldini D. Banfield W. B. Banerdt (2021). Forward Modeling of the Phobos Tides and applications to the first Martian year of the InSight mission. *Earth and Space Science*, 8, e2021EA001669
- Putzig, N. E., & Mellon, M. T. (2007). Apparent thermal inertia and the surface heterogeneity of Mars. *Icarus*, 191(1), 68-94.
- Pike, W. T., U. Staufer, M. H. Hecht, W. Goetz, D. Parrat, H. Sykulska-Lawrence, S. Vijendran, and M. B. Madsen (2011), Quantification of the dry history of the Martian soil inferred from in situ microscopy, *Geophysical Research Letters*, 38, L24201.
- Santamarina J.C., K.A. Klein, M.A. Fam, *Soils and Waves* (Wiley, New York, 2001)
- Sollberger, D., Schmelzbach, C., Andersson, F., Robertsson, J. O. A., Brinkman, N., Kedar, S., et al. (2021). A reconstruction algorithm for temporally aliased seismic signals recorded by the InSight Mars lander. *Earth and Space Science*, e2020EA001234.
- Spiga, A., Murdoch, N., Lorenz, R., Forget, F., Newman, C., Rodriguez, S., et al. (2020). A study of daytime convective vortices and turbulence in the martian Planetary Boundary Layer based on half-a-year of InSight atmospheric measurements and Large-Eddy Simulations. *Journal of Geophysical Research: Planets* 125, e2020JE006511.
- Spohn, T., Grott, M., Smrekar, S. E., Knollenberg, J., Hudson, T. L., Krause, C., et al. (2018). The heat flow and physical properties package (HP<sup>3</sup>) for the InSight mission. *Space Science Reviews*, 214(5), 96.
- Spohn T., Hudson T., Marteau E. et al (2021a) The HP<sup>3</sup> penetrator (Mole) on Mars: Soil properties derived from the penetration attempts and related activities. Submitted to *Space Science Reviews*, <http://arxiv.org/abs/2112.04438>
- Spohn, T., Hudson, T., Witte, L. et al (2021b) The InSight HP<sup>3</sup> mole on Mars: Lessons Learned from attempts to penetrate to depth in the Martian soil. *Advanced Space Research*, in press, <http://arxiv.org/abs/2112.03234>
- Stähler R.C., R. Widmer-Schmidrig, J.-R. Scholz, M. van Driel, A. Mittelholz, K. Hurst, et al. (2020). Geophysical Observations of Phobos Transits by InSight. *Geophysical Research Letters*, 47, e2020GL089099.
- Trebi-Ollennu A, W Kim, K Ali et al (2018). InSight Mars Lander Robotics Instrument Deployment System. *Space Science Reviews*, doi: 10.1007/s11214-018-0520-7
- Verdier, N., Ansan-Mangold V., Delage P., et al. (2022). Using wind dispersion effects during the InSight tether burial activities to better constrain the regolith grain size distribution. *In prep*.
- Viudez-Moreiras D, Newman, CE, Forget, F, Lemmon, M, Banfield, D et al. (2020). Effects of a Large Dust Storm in the Near-Surface Atmosphere as Measured by InSight in Elysium Planitia, Mars. Comparison With Contemporaneous Measurements by Mars Science Laboratory, *Journal of Geophysical Research: Planets*, (125) 9, e2020JE006493.
- Walton O.R., De Moor P. C., Gill K.S. (2007). Effects of gravity on cohesive behavior of fine powders: implications for processing Lunar regolith. *Granular Matter* 9:353-363.
- Warner N. H., M.P. Golombek, V. Ansan, E. Marteau, N. Williams et al. (2022a). In-situ and orbital stratigraphic observations from the insight landing site, Mars. *53rd Lunar and Planetary Science Conference*, Houston, USA.
- Warner, N.H., Golombek, M.P., Ansan, V., Marteau, E., Williams, N. et al. (2022b). In Situ and Orbital Stratigraphic Characterization of the InSight Landing Site – The Type Example of a Regolith-Covered Lava Plain on Mars. Submitted to *Journal of Geophysical Research: Planets*.